Dynamic Response Analysis of DC–DC Converter With Supercapacitor for Direct Borohydride Fuel Cell Power Conditioning System

Tai-Sik Hwang, *Student Member, IEEE*, Matthew James Tarca, *Student Member, IEEE*, and Sung-Yeul Park, *Member, IEEE*

***Abstract*—The direct borohydride fuel cell (DBFC) is directly fed sodium borohydride as a fuel and hydrogen peroxide as an oxidant. The output voltage of the DBFC varies with respect to current demand. Therefore, it requires a dc–dc converter for a regulated output voltage. The dc–dc converter should be designed considering both the impact of the fuel cell and load disturbances to achieve wide range voltage regulation. This paper analyzes the impact of the DBFC impedance on the dc–dc converter. Based on the converter's small signal model including the DBFC impedance, the boost converter was evaluated. Impacts of the voltage and current control loops on the boost converter were investigated. Improved response time and stability of the DBFC dc–dc converter were observed by adding a supercapacitor between the DBFC and the dc–dc converter. Finally, two converter controllers, a nonlinear feedforward controller and a state feedback controller are proposed for further improvement of the dc–dc converter response time. A prototype 20-W dc–dc converter was built and tested to show the response improvement of the proposed analysis and control scheme.**

***Index Terms*—Boost converter, direct borohydride fuel cell (DBFC), dc–dc converter, supercapacitor.**

I. Introduction

MOST fuel cell power converters are expected to produce power on demand, also known as load following power sources. However, the response time of the fuel cells is typically known to be slower than those of other power sources such as batteries and diesel engines. This is because of the operation of the balance of plant (BOP) associated with mass and heat balances inside and outside the stack. In order to improve the response time, many fuel cell systems are combined with a battery or capacitor to form a hybrid power generation system [1], [2].

A bidirectional dc–dc converter, which is used to interface an ultracapacitor as energy storage to a fuel cell, was presented in [3] and [4]. These papers have shown that the bidirectional converter with the ultracapacitor had better control response times for a fuel cell system during voltage transients. Jin *et al*. [5] and Liu *et al*. [6] proposed a novel hybrid fuel cell power conditioning system. This system consists of the fuel cell, a battery, a unidirectional dc–dc converter, a bidirectional dc–dc converter, and a dc–ac inverter. A fuel cell and a battery are connected to the common dc bus for the unidirectional dc–dc converter and the bidirectional dc–dc converter.

Harfman-Todorovic *et al*. and Itoh and Hayashi reviewed some of the characteristics of fuel cell applications. A discussion of important considerations for fuel cell converter design is presented. The role of the fuel cell controller was briefly introduced. Todorovic *et al*. focused on the design of a dc–dc converter, control, and auxiliary energy storage system. A novel converter configuration, which improves utilization of the high-frequency transformer and simplifies the overall system control, was proposed.

Stability analysis of fuel cell powered dc–dc converters was also discussed in [10]. An equivalent circuit model based on the chemical reactions inside of the fuel cell was presented. It showed that fuel cell internal impedance can significantly affect the dynamics of the dc–dc converter. Also, the behavior of the fuel cell during purging has been discussed. In order to overcome these problems, the supercapacitor connected in parallel with the fuel cell was proposed. An impedance analysis approach had been proposed in [11] and [12]. It showed the static response of the overall system with the fuel cell and the dc–dc converter. However, it did not clearly show the impact of the individual components.

In [13] and [14], the input impedance of the boost power factor correction converter for both the conventional current controller and the duty ratio feedforward controller were explained theoretically. Due to the nonlinearity and unstable zero dynamics of the boost converter, it has some limitations such as low bandwidth (BW) and poor dynamic response [15], [16]. In order to solve this drawback, a novel nonlinear control strategy based on input–output feedback linearization was proposed in [17] and [18].

The direct borohydride fuel cell (DBFC) is directly fed sodium borohydride as fuel and hydrogen peroxide as oxidant. The output voltage of the DBFC varies with respect to current demand. In order to regulate the output voltage constantly for autonomous operation, the pump to supply solutions to the DBFC stack needs to be controlled. Therefore, the controllers

Manuscript received August 23, 2011; revised November 7, 2011; accepted January 4, 2012. Date of current version April 20, 2012. A preliminary version of this paper was presented at the 8th International Conference on Power Electronics—ECCE Asia (ICPE 2011-ECC Asia). This work was supported by Northeast Utilities Company. Recommended for publication by Associate Editor S. Choi.

T.-S. Hwang, M. J. Tarca, and S.-Y. Park are with the Department of Electrical and Computer Engineering, University of Connecticut, Storrs, CT 06269-2157 USA (e-mail: tai-sik.hwang@engr.uconn.edu; matt.tarca@gmail.com).

Color versions of one or more of the figures in this paper are available online at http://ieeexplore.ieee.org.

Digital Object Identifier 10.1109/TPEL.2012.2185711

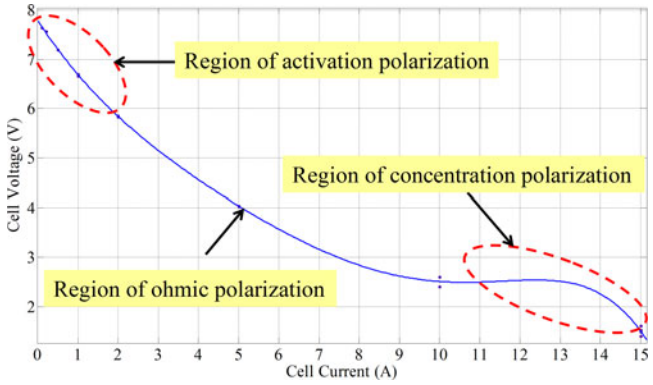

Fig. 1. *V–I* characteristics of the DBFC.

of the balance of plant for the DBFC will be implemented with a microcontroller. By implementing the BOP with the flexible digital controller, control responses can be improved [19].

In this paper, a dynamic response analysis is described. Based on the fuel cell source model, inner current and outer voltage control loop responses are explained in the frequency domain in order to analyze the impact of the individual components. By adding the supercapacitor, the response time of the voltage control loop will be improved. In addition, a nonlinear feedforward control and a state feedback control are proposed to increase the BW of the control loop. A 20-W prototype DBFC power conditioning system was built and used to verify the proposed analysis approach and control scheme.

II. System Modeling

A. *V–I* Characteristics of DBFC

Fig. 1 shows the *V–I* characteristics of the DBFC. It can be seen that if the initial nonlinearity (activation polarization) and high-current region (concentration polarization) are neglected, the DBFC works in a nearly linear region (ohmic polarization). Considering the linear region, the DBFC voltage is variable from 4 to 8 V [20].

B. Frequency Response of the DBFC

Fig. 2(a) shows the frequency domain response of the DBFC [20] impedance with different constant current load conditions with an ac sweep frequency range of 1 Hz to 20 kHz. Fig. 2(b) shows the corresponding Nyquist plot. Fig. 3 shows the equivalent circuit of the DBFC.

Fig. 4 shows the Bode plot of the DBFC impedance calculated by $Z_{fc}(s)$ which is given by (1). If an operating range of the boost converter is from 100 Hz to 10 kHz with respect to the BW and a sampling time, the DBFC naturally has a slow frequency response with respect to the gain and phase. Therefore, a transient response can be considered as a constant value. Furthermore, the total impedance of the DBFC can be simplified with a constant resistor for fast frequency responses.

From Fig. 3, the impedance of the DBFC is given as

$$Z_{fc}(s) = \left.\frac{R_1R_2C_1s + R_1 + R_2}{R_1C_1s + 1}\right|_{100\text{Hz}<f<10\text{kHz}} \simeq R_{fc} \quad (1)$$

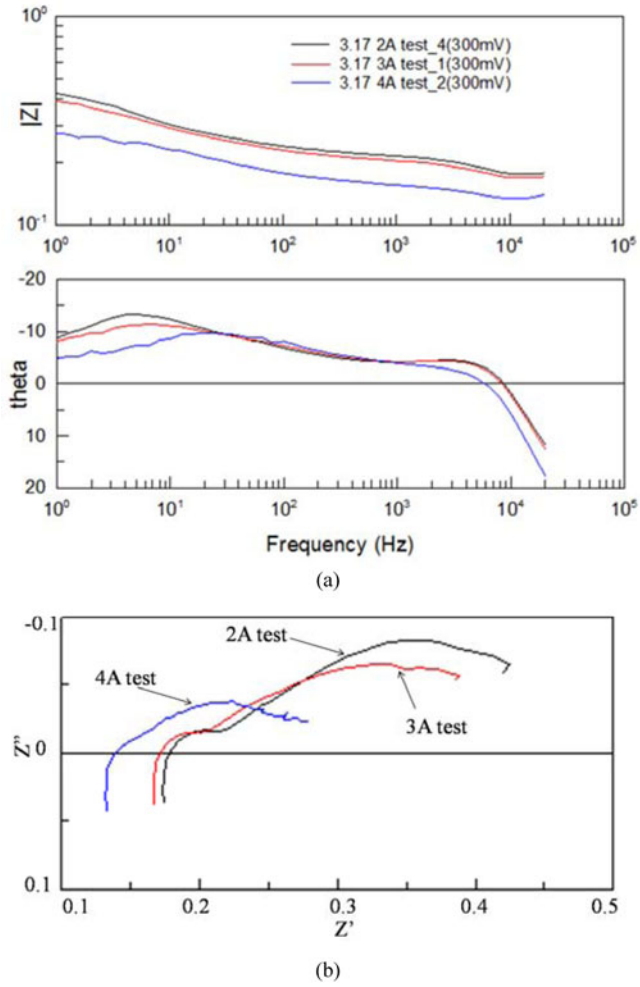

Fig. 2. Measured frequency response data of the DBFC. (a) Frequency domain response of the DBFC. (b) Nyquist plot of the DBFC.

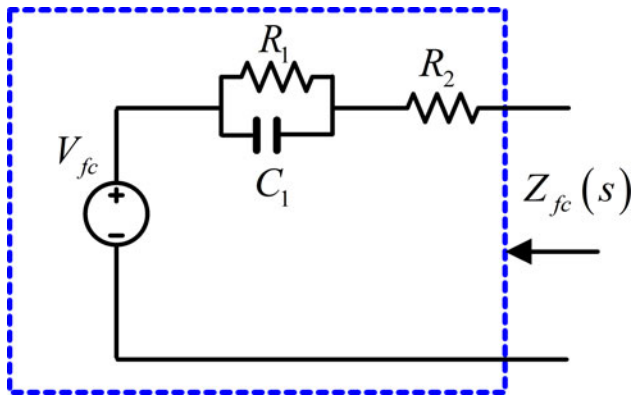

Fig. 3. Equivalent circuit of the DBFC.

where R_1, R_2, C_1, and R_{fc} are impedance parameters of the DBFC. R_{fc} is about 0.3–0.6 Ω.

C. Boost Converter Modeling

Fig. 5 shows the configuration of the DBFC system. The boost converter is connected to the DBFC. The converter output

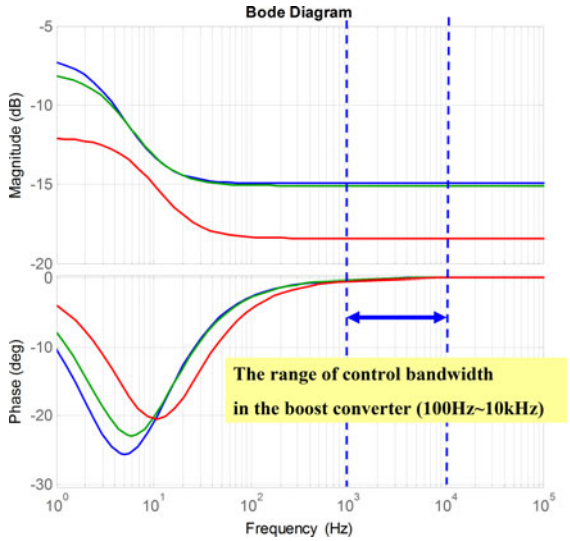

Fig. 4. Bode plot of the DBFC impedance.

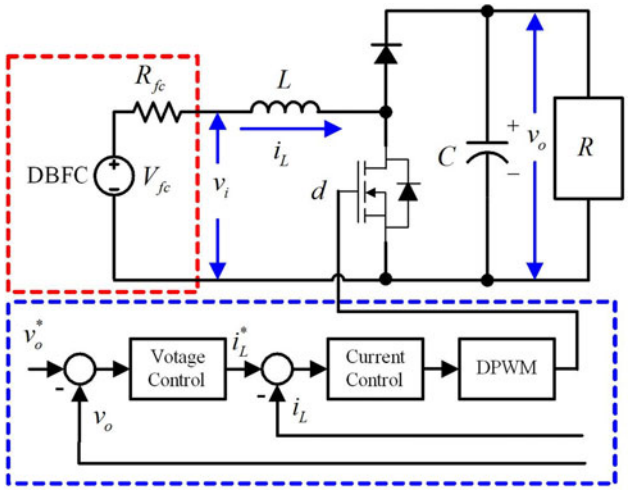

Fig. 5. DBFC boost converter configuration.

voltage is 12 V and the rated power is 20 W. The control scheme of the boost converter consists of a current control in the inner loop and a voltage control in the outer loop. A digital controller for a current and a voltage loops is designed. Frequency analysis for the response time is considered in the continuous domain (s-domain) because it is easy to understand physically. However, an implementation of the digital controller considers the impacts of sampling time. Therefore, the maximum control BW is limited by the sampling time (10 kHz).

Equations based on the average model of the boost converter are given by

$$V_{fc} - R_{fc} i_L = v_i \tag{2}$$

$$L\frac{di_L}{dt} = v_i - (1-d)\, v_o \tag{3}$$

$$C\frac{dv_o}{dt} = (1-d)\, i_L - \frac{v_o}{R} \tag{4}$$

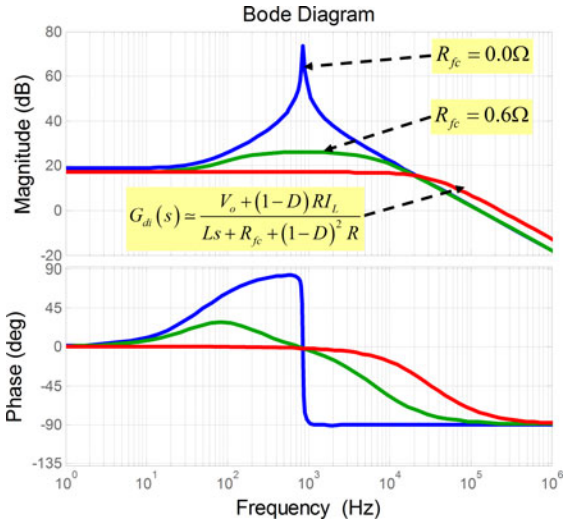

Fig. 6. Bode plot of the duty ratio-to-inductor current transfer function with respect to R_{fc}.

where V_{fc} is the DBFC voltage, d is the on-duty cycle of switch, v_i is the input voltage, i_L is the inductor current, v_o is the output voltage, L is the inductor, C is the filter capacitor, and R is the load resistor.

Hence, small-signal equation models are written as

$$\tilde{v}_i = -R_{fc}\tilde{i}_L \tag{5}$$

$$L\frac{d\tilde{i}_L}{dt} = \tilde{v}_i - (1-D)\,\tilde{v}_o + \tilde{d}V_o \tag{6}$$

$$C\frac{d\tilde{v}_o}{dt} = -\tilde{d}I_L + (1-D)\,\tilde{i}_L - \frac{\tilde{v}_o}{R} \tag{7}$$

where $\tilde{d}$ is the ac signal of on-duty cycle of switch, $\tilde{v}_i$ is the ac signal of the input voltage, $\tilde{i}_L$ is the ac signal of the inductor current, $\tilde{v}_o$ is the ac signal of output voltage, D is the dc component of the on component of the duty cycle of the switch, V_o is the dc component of the output voltage, and I_L is the dc component of the inductor current.

III. Response Analysis of DBFC DC–DC Converter

A. Frequency Response of Boost Converter With Respect to the Impedance of the DBFC

The duty ratio-to-inductor current transfer function $G_{di}(s)$ can be calculated as

$$G_{di}(s) \triangleq \frac{\tilde{i}_L}{\tilde{d}} = \frac{RCV_o s + V_o + (1-D)\,RI_L}{RLCs^2 + (L + R_{fc}RC)\,s + R_{fc} + (1-D)^2 R}. \tag{8}$$

Fig. 6 shows the Bode plot of the duty ratio-to-inductor current transfer function with respect to R_{fc}. If the impedance is a zero, the DBFC appears as an ideal dc source.

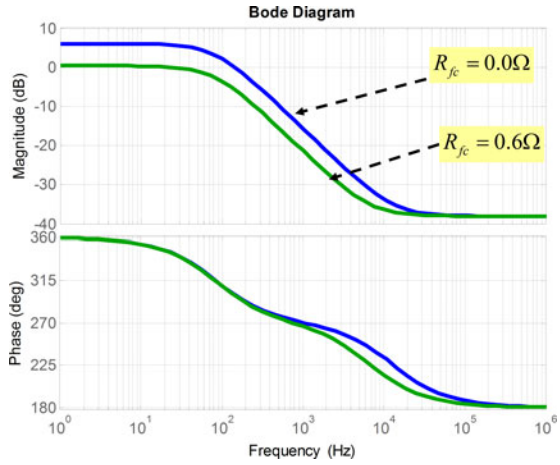

Fig. 7. Bode plot of inductor current-to-output voltage transfer function with respect to R_{fc}.

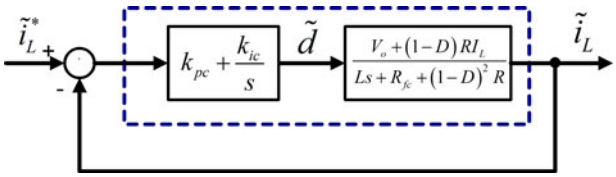

Fig. 8. Current control block diagram.

From (8), the duty ratio-to-inductor current transfer function can be simplified as

$$G_{di}(s) \simeq \frac{V_o + (1-D)RI_L}{Ls + R_{fc} + (1-D)^2 R}. \tag{9}$$

The inductor current-to-output voltage transfer function $G_{iv}(s)$ can be expressed as

$$G_{iv}(s) \triangleq \frac{\tilde{v}_o}{\tilde{i}_L} = \frac{-Ls - R_{fc} + (1-D)^2 R}{(RCs+2)(1-D)}. \tag{10}$$

Fig. 7 shows the Bode plot of inductor current-to-output voltage transfer function with respect to R_{fc}. From Figs. 6 and 7, gains and phases of this transfer function in the frequency domain are different according to the DBFC impedance. Therefore, they impact the response time of the voltage and current loops. This paper intends to explain the impact of these factors in the voltage and current control loops.

B. Impact of the DBFC Impedance With Conventional Current and Voltage Control

Fig. 8 shows the current control block diagram for the DBFC boost converter, where the proportional integrator (PI) control gains are $k_{pc} = L\omega_c/V_t$ and $k_{ic} = \left(R_{fc} + (1-D)^2 R\right)\omega_c/V_t$ where $V_t = V_o + (1-D)RI_L$.

The closed-loop transfer function is given as

$$\frac{\tilde{i}_L^*}{\tilde{i}_L} = \frac{k_{pc}V_t/Ls + k_{ic}V_t/L}{s^2 + (R_{fc} + k_{pc}V_t)/Ls + k_{ic}V_t/L} = \frac{\omega_c}{s+\omega_c}. \tag{11}$$

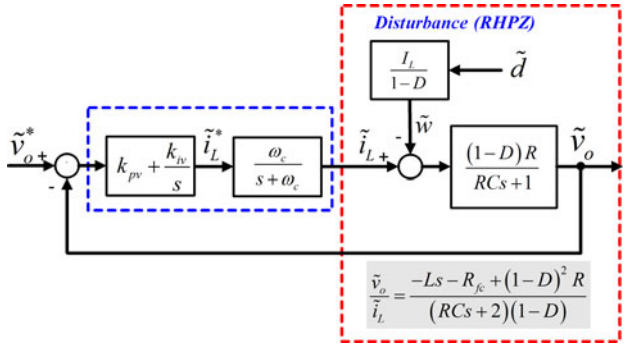

Fig. 9. Voltage control block diagram.

The reference current-to-duty ratio transfer function is calculated as

$$\frac{\tilde{d}}{\tilde{i}_L^*} = \frac{1}{V_o}\frac{\omega_c}{s+\omega_c}\left(Ls + R_{fc} + (1-D)^2 R\right). \tag{12}$$

Fig. 9 is the voltage control block diagram, where PI control gains are $k_{pv} = C\omega_v/(1-D)$ and $k_{iv} = \omega_v/R(1-D)$.

The closed-loop transfer function is given as

$$\frac{\tilde{v}_o}{\tilde{v}_o^*} = \frac{\omega_v\omega_c}{(s+\omega_v)(s+\omega_c)} \simeq \frac{\omega_v}{s+\omega_v}(\omega_c \gg \omega_v) \tag{13}$$

The disturbance of the voltage control can be expressed as

$$\tilde{w} = -\frac{I_L}{(1-D)V_o}\frac{\omega_c}{s+\omega_c}\left(Ls + R_{fc} + (1-D)^2 R\right)\tilde{i}_L^*. \tag{14}$$

Fig. 10 shows the step response of the disturbance with voltage control. If R_{fc} is equal to zero, it means the power source is ideal. However, in the real case, R_{fc} will be some value with respect to the fuel cell impedance. If the value of R_{fc} is increased, then it affects the disturbance factor as well. This disturbance factor comes from a right half-plane zero (RHPZ) in typical boost converters. Therefore, the voltage control will have a slow response with respect to disturbances. Therefore, the boost converter as an ideal dc source is better than that with the DBFC in order to achieve a faster response.

IV. Response Improvement With Addition of Supercapacitor

Fig. 11 shows the DBFC boost converter with the addition of the supercapacitor.

The equations of the small-signal model are expressed as

$$(R_{fc} + R_s)C_s\frac{d\tilde{v}_i}{dt} + R_sR_{fc}C_s\frac{d\tilde{v}_i}{dt} = -\tilde{v}_i - R_{fc}\tilde{i}_L \tag{15}$$

$$L\frac{d\tilde{i}_L}{dt} = \tilde{v}_i - (1-D)\tilde{v}_o + \tilde{d}V_o \tag{16}$$

$$C\frac{d\tilde{v}_o}{dt} = -\tilde{d}I_L + (1-D)\tilde{i}_L - \frac{\tilde{v}_o}{R} \tag{17}$$

where C_s is the supercapacitor, and R_s is the equivalent series resistor (ESR) of the supercapacitor.

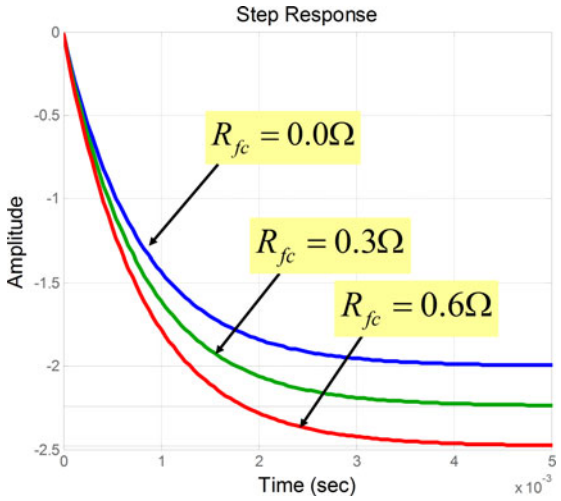

Fig. 10. Step response of the disturbance in the voltage control.

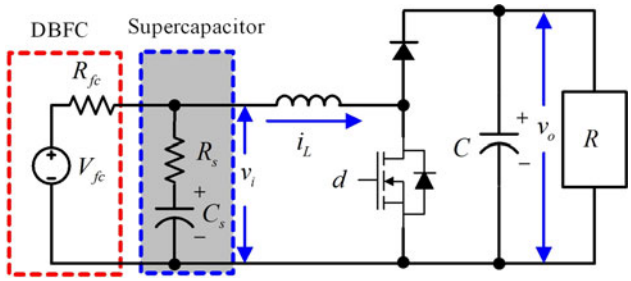

Fig. 11. DBFC boost converter adding supercapacitor.

From (15) to (17), the duty ratio-to-inductor current transfer function with the supercapacitor is given as

$$G_{di\_cap}(s) \triangleq \frac{\tilde{i}_L}{\tilde{d}} = \frac{a_2 s^2 + a_1 s + a_0}{b_3 s^3 + b_2 s^2 + b_1 s + b_0}. \qquad (18)$$

where $a_2, a_1, a_0, b_3, b_2, b_1,$ and b_0 are constant.

Fig. 12 shows the Bode plot of the duty ratio-to-inductor current transfer function with the supercapacitor. Previously, it was shown that the DBFC impedance can make the response time with voltage control slow. By adding the supercapacitor, the impact of the DBFC impedance can be minimized in order to increase the response time. The resonance frequency in the duty ratio-to-inductor current transfer function $G_{di\_cap}(s)$ depends on the value of the supercapacitor. If $G_{di\_cap}(s)$ is close to the resonance frequency of the duty ratio-to-inductor current transfer function $G_{di}(s)$ without the supercapacitor then the DBFC with the addition of the supercapacitor approximates an ideal dc source which has an improved voltage response as seen in Fig. 6. This supercapacitor is not only an energy buffer, but also has the function of transient response improvement. By frequency analysis, the minimum value of the supercapacitor can be determined.

In Figs. 6 and 12, the duty ratio-to-inductor current with supercapacitor transfer function is closed to that of ideal dc source. This condition is as follows:

$$G_{di\_cap}(s)|_{C_s=1.5\ F} \cong G_{di}(s)|_{R_{fc}=0\ \Omega}. \qquad (19)$$

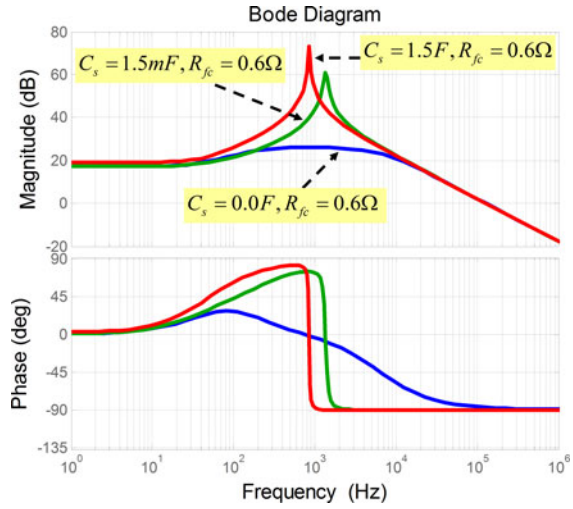

Fig. 12. Bode plot of duty ratio-to-inductor current transfer function with supercapacitor.

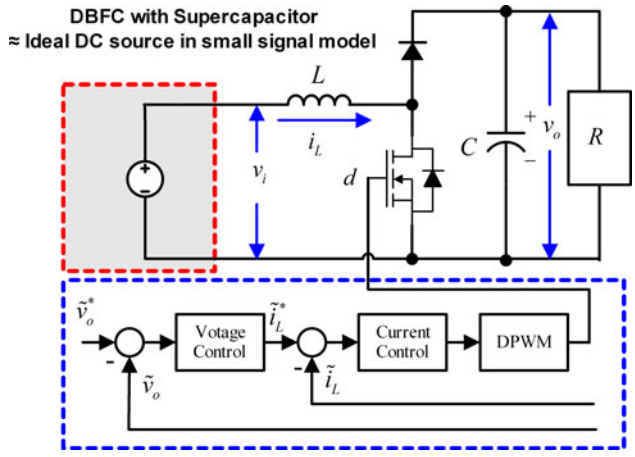

Fig. 13. DBFC boost converter configuration with addition of supercapacitor.

V. Further Response Improvement

A. Limitation of Conventional PI Control

Fig. 13 shows the DBFC boost converter configuration having added the supercapacitor. It consists of the DBFC, the supercapacitor, and the boost converter with the conventional PI control, which has the current control in inner loop and voltage control in outer loop. The time constant with respect to the supercapacitor ESR and supercapacitor is much slower than the controller response time during the ESR voltage drop. Therefore, the DBFC with the supercapacitor can be equivalent to the ideal dc source in small signal model when considering the system dynamics.

Transfer functions of the boost converter with a supercapacitor, which is considered an ideal dc source, are given as

$$\frac{\tilde{i}_L}{\tilde{d}} \simeq \frac{RCV_o s + V_o + (1-D) I_L R}{RLCs^2 + Ls + (1-D)^2 R} \qquad (20)$$

$$\frac{\tilde{v}_o}{\tilde{i}_L} \simeq \frac{-RI_L Ls + (1-D) V_o R}{RCV_o s + V_o + (1-D) I_L R}. \qquad (21)$$

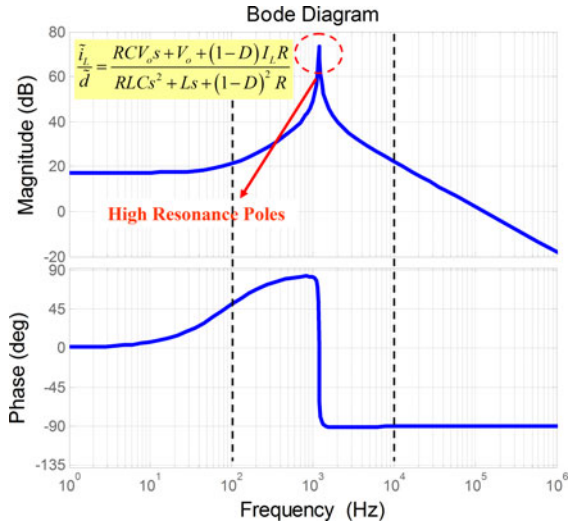

Fig. 14. Bode plot of duty ratio-to-inductor current transfer function of DBFC boost converter adding supercapacitor.

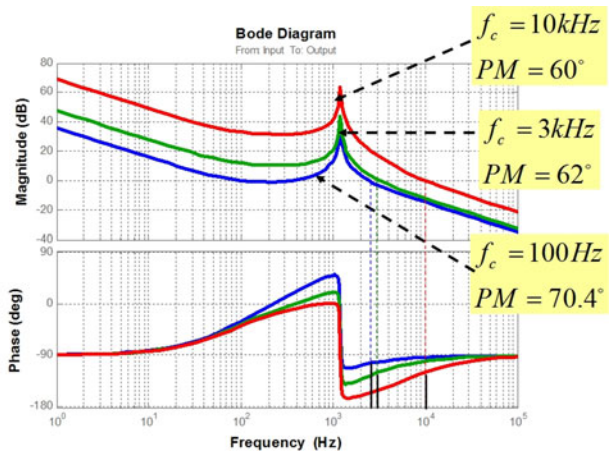

Fig. 15. Bode plot of open loop with PI current control.

Fig. 14 shows the Bode plot of transfer functions of the DBFC boost converter after adding supercapacitor. The conventional PI control approach has two limitations in case of achieving a high BW.

First, the system has a high-resonance pole in the duty ratio-to-inductor current transfer function with respect to the current controller design [21]–[26]. In order to avoid it, the control parameters such as poles and zeros should be allocated in either to the right side or to the left side of the resonance point. However, the right side needs to consider a sampling time of the digital controller (10–20 kHz). In the case of the sampling time from 10 to 20 kHz, it is difficult to place the control parameters on the right side.

Second, it has the RHPZ in the inductor current-to-output voltage transfer function with respect to the voltage controller design in (21) [27]–[30]. The RHPZ makes achieving high BW in the voltage loop difficult. Previously, by adding the supercapacitor, the disturbance due to the RHPZ was minimized.

Fig. 15 shows the Bode plot of the open-loop transfer function with a PI-controlled current loop according to BWs and phase margins. The designed phase margin (PM) is 60°. Also, the bandwidth (BW) is designed from 1 to 10 kHz. Because the sampling time is 10 kHz, the target BW of the current control is limited under 1 kHz in the case of the digital controller. However, it is very difficult to obtain BW = 1 kHz, PM = 60° because of the high resonance pole. In order to avoid an unstable point, the final designed BW is 100 Hz. This means that the conventional method will greatly limit the BW when designing the digital current controller because of the high resonance pole. Moreover, the voltage controller should have even lower BW, under 10 Hz. Therefore, in the case of the conventional approach, the analogue control is designed or the resonance pole is moved by replacement of the parameter such as the inductor and capacitor.

B. Current Control With High Bandwidth by Nonlinear Feedforward in Inner Loop

In order to cancel the high-resonance pole, a nonlinear feedforward scheme was proposed in [13], [14]. With this method, the duty ratio of the boost converter is calculated as

$$d = \frac{v_o - v_i + v_c}{v_o} = 1 - \frac{v_i}{v_o} + \frac{v_c}{v_o} \tag{22}$$

where v_c is the controller output.

Then, equations in the average model are expressed as

$$L\frac{di_L}{dt} = v_c \tag{23}$$

$$C\frac{dv_o}{dt} = \frac{v_i}{v_o}i_L - \frac{v_c}{v_o}i_L - \frac{v_o}{R}. \tag{24}$$

Hence, equations in the small-signal model are written as

$$L\frac{d\tilde{i}_L}{dt} = \tilde{v}_c \tag{25}$$

$$C\frac{d\tilde{v}_o}{dt} = \frac{V_i}{V_o}\tilde{i}_L - \frac{2}{R}\tilde{v}_o - \frac{I_L}{V_o}\tilde{v}_c + \frac{I_L}{V_o}\tilde{v}_i. \tag{26}$$

By (23)–(26), transfer functions of the boost converter with nonlinear feedforward are given as

$$\frac{\tilde{i}_L}{\tilde{v}_c} = \frac{1}{Ls} \tag{27}$$

$$\frac{\tilde{v}_o}{\tilde{i}_L} = \frac{-I_L LRs + V_i R}{V_o RCs + 2V_o} \tag{28}$$

$$\frac{\tilde{v}_o}{\tilde{v}_c} = \frac{-I_L Ls + V_i}{V_o Ls\,(RCs + 2)}. \tag{29}$$

Fig. 16 shows the Bode plot of transfer functions of the boost converter with nonlinear feedforward control. The duty ratio-to-inductor current transfer function shown in Fig. 16 is simplified to an integrator form. It is free to design the current controller with a high BW.

Fig. 17 shows the block diagram of a proposed current control with nonlinear feedforward. By using the nonlinear feedforward,

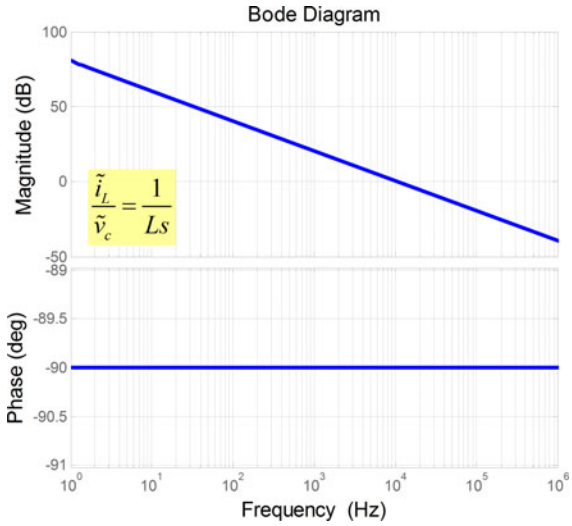

Fig. 16. Bode plot of duty-to-current transfer function of boost converter by nonlinear feedforward.

the plant can be simplified as (23). The control gains are $k_{pc} = L\omega_c$, $k_{ic} = \hat{R}\omega_c$ and $k_{vc} = \hat{R}$.

Then, the overall closed-loop transfer function becomes

$$\frac{\tilde{i}_L^*}{\tilde{i}_L} = \frac{k_{pc}/Ls + k_{ic}/L}{s^2 + (k_{vc} + k_{pc})/Ls + k_{ic}/L} = \frac{\omega_c\left(s + \hat{R}\right)}{(s + \omega_c)\left(s + \hat{R}\right)} = \frac{\omega_c}{s + \omega_c}. \tag{30}$$

C. Voltage Control With Fast Response Time by Using State Feedback Control

The inductor current-to-output voltage transfer function shown in (28) still has the RHPZ. Therefore, it makes a high-BW design difficult for the conventional voltage controller design. Based on the state feedback control, the RHPZ can be compensated. The state feedback control will minimize the impact of RHPZ using two states, which are the output voltage and inductor current. Its output will be the current reference of previous current control with the nonlinear feedforward. Finally, the proposed method consists of the current loop with the nonlinear feedforward in inner loop and the voltage loop by the state feedback control in outer loop.

From (30), the state equation with respect to the current loop is given as

$$\frac{d\tilde{i}_L}{dt} = -\omega_c\tilde{i}_L + \omega_c\tilde{i}_L^*. \tag{31}$$

From (25) and (26), the state equation with respect to the voltage loop is given as

$$\frac{d\tilde{v}_o}{dt} = \frac{V_i}{CV_o}\tilde{i}_L - \frac{2}{RC}\tilde{v}_o - \frac{I_L L}{CV_o}\frac{d\tilde{i}_L}{dt} + \frac{I_L}{CV_o}\tilde{v}_i. \tag{32}$$

Based on previous analysis, the impact of the DBFC with the supercapacitor will be minimized, which means the input variation is around zero ($\tilde{v}_i \simeq 0$).

Hence, the input term can be ignored.

$$\frac{d\tilde{v}_o}{dt} = \frac{V_i}{CV_o}\tilde{i}_L - \frac{2}{RC}\tilde{v}_o - \frac{I_L L}{CV_o}\frac{d\tilde{i}_L}{dt}. \tag{33}$$

Combining (31) and (33), final state equation is expressed as

$$\frac{d\tilde{v}_o}{dt} = \frac{(V_i + \omega_c L I_L)}{CV_o}\tilde{i}_L - \frac{2}{RC}\tilde{v}_o - \frac{\omega_c L I_L}{CV_o}\tilde{i}_L^*. \tag{34}$$

The state variables are

$$\mathbf{x} = [\,x_1 \quad x_2\,]^T, \quad x_1 = \tilde{i}_L, \quad x_2 = \tilde{v}_o, \quad u = i_L^*. \tag{35}$$

The overall state space model can then be obtained as

$$\begin{bmatrix}\dot{x}_1\\ \dot{x}_2\end{bmatrix} = \begin{bmatrix}-\omega_c & 0\\ \dfrac{(V_i + \omega_c L I_L)}{CV_o} & -\dfrac{2}{RC}\end{bmatrix}\begin{bmatrix}x_1\\ x_2\end{bmatrix} + \begin{bmatrix}\omega_c\\ -\dfrac{\omega_c L I_L}{CV_o}\end{bmatrix}u$$
$$y = x_2. \tag{36}$$

The proposed state feedback control law is given as

$$u = (r - x_2)\frac{k_a}{s} + [\,k_1 \quad k_2\,]\begin{bmatrix}x_1\\ x_2\end{bmatrix}. \tag{37}$$

The control gain can be computed by a pole placement [23]. Therefore, the system eigenvalues (poles) are designed as

$$\Delta_f(s) = \det\begin{bmatrix}s\mathbf{I} - \mathbf{A} - \mathbf{bK} & -\mathbf{b}k_a\\ \mathbf{c} & s\end{bmatrix} = (s + p)^3 \tag{38}$$

where p is a designed pole.

$$\mathbf{A} = \begin{bmatrix}-\omega_c & 0\\ \dfrac{(V_i + \omega_c L I_L)}{CV_o} & -\dfrac{2}{RC}\end{bmatrix}, \quad \mathbf{b} = \begin{bmatrix}\omega_c\\ -\dfrac{\omega_c L I_L}{CV_o}\end{bmatrix},$$
$$\mathbf{c} = [\,0 \quad 1\,], \quad \mathbf{K} = [\,k_1 \quad k_2\,].$$

D. Closed Transfer Function of Proposed Control System

In (37), the control input can be rewritten as

$$u = r_a + \mathbf{Kx}, \quad r_a = (r - x_2)\frac{k_a}{s}. \tag{39}$$

The transfer function from r_a to y is given as

$$G(s) = \frac{N(s)}{D(s)} = \mathbf{c}\,(s\mathbf{I} - \mathbf{A} - \mathbf{bk})^{-1}\,\mathbf{b}. \tag{40}$$

And the closed transfer function [31] from r to y becomes

$$G_{ry}(s) = \frac{k_a N(s)}{\Delta_f(s)}. \tag{41}$$

The state feedback does not affect the zeros of the plant transfer function. However, if the current controller has a high BW than it can be assumed as

$$\frac{\tilde{i}_L^*}{\tilde{i}_L} = \frac{\omega_c}{s + \omega_c} \simeq 1. \tag{42}$$

From (36), the transfer function from u to y expressed as

$$G_{uy}(s) = \mathbf{c}\,(s\mathbf{I} - \mathbf{A})^{-1}\,\mathbf{b} \simeq \frac{(V_i + \omega_c L I_L) - \omega_c L I_L}{CV_o\,(s + (2/RC))} = \frac{V_i}{CV_o\,(s + (2/RC))}. \tag{43}$$

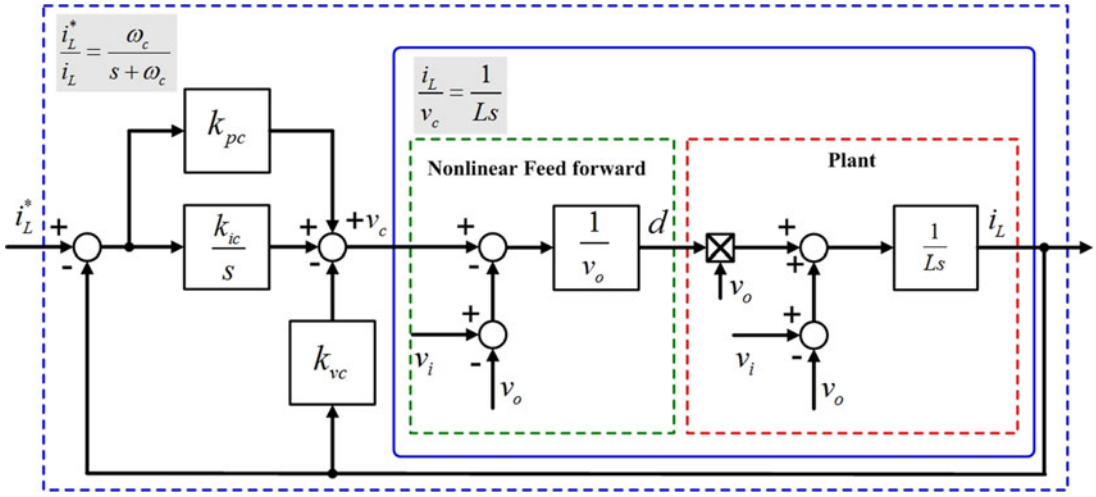

Fig. 17. Block diagram of proposed current control with nonlinear feedforward.

Hence, the RHPZ can be ignored in the current control with a high BW.

Finally, the closed transfer function from r to y can be approximated as

$$G_{ry}(s) \simeq \frac{p^3}{(s+p)^3}. \tag{44}$$

Fig. 18 shows a proposed state feedback control block diagram for the voltage control. The inner loop looks like a first-order low-pass filter given by (30). In the proposed control scheme, the PI current controller with high BW by using the nonlinear feedforward is the inner loop. The voltage controller, which is the state feedback law, is the outer loop.

E. Stability of Proposed Controllers

From (23) and (24), the nonlinear plant is given as

$$\dot{z}_1 = \frac{u}{L} \tag{45}$$

$$\dot{z}_2 = \frac{v_i}{C}\frac{z_1}{z_2} - \frac{1}{C}\frac{uz_1}{z_2} - \frac{1}{R}z_2. \tag{46}$$

The state variables are

$$z_1 = i_L, \quad z_2 = v_o, \quad u = i_L^*. \tag{47}$$

From Fig. 17, the current controller is given as

$$u = k_{pc}(z_1^* - z_1) + k_{ic}\int (z_1^* - z_1)\,dt - k_{vc}z_1. \tag{48}$$

Substituting (42) into (39), the result is the same as (31).

$$\begin{aligned}\dot{z}_1 &= \frac{k_{pc}}{L}(z_1^* - z_1) + \frac{k_{ic}}{L}\int (z_1^* - z_1)\,dt - \frac{k_{vc}}{L}z_1 \\ &= \omega_c(z_1^* - z_1) + \frac{\hat{R}}{L}\omega_c\int (z_1^* - z_1)dt - \frac{\hat{R}}{L}z_1\end{aligned} \tag{49}$$

$$\ddot{z}_1 + \omega_c\dot{z}_1 - \omega_c\dot{z}_1^* = -\frac{\hat{R}}{L}(\dot{z}_1 + \omega_c z_1 - \omega_c z). \tag{50}$$

Initial state variables are

$$\dot{z}_1(0) = 0, \quad z_1(0) = 0, \quad z_1^*(0) = 0, \quad z_2(0) = v_i. \tag{51}$$

Hence,

$$\dot{z}_1 = -\omega_c z_1 + \omega_c z_1^*. \tag{52}$$

From (46) and (52), the nonlinear plant including the current loop can be rewritten as

$$\dot{z}_1 = -\omega_c z_1 + \omega_c w \tag{53}$$

$$\begin{aligned}\dot{z}_2 &= \frac{v_i}{C}\frac{z_1}{z_2} - \frac{L}{C}\frac{z_1\dot{z}_1}{z_2} - \frac{1}{R}z_2 \\ &= \frac{v_i}{C}\frac{z_1}{z_2} + \frac{L\omega_c}{C}\frac{z_1^2}{z_2} - \frac{L\omega_c}{C}\frac{z_1 w}{z_2} - \frac{1}{R}z_2\end{aligned} \tag{54}$$

where the control input is the current reference ($w = z_1^* = i_L^*$).

From Fig. 18, the voltage controller can be written as

$$w = k_a\int (z_2^* - z_2)dt + k_1 z_1 + k_2 z_2. \tag{55}$$

In (54), the first term is the integrator controller. If the state feedback gains (k_1, k_2) guaranty stability in (53) and (54), then the stable integrator gain k_a will be determined.

The state feedback control law without the integrator becomes

$$w = k_1 z_1 + k_2 z_2. \tag{56}$$

Substituting (56) into (53) and (54),

$$\dot{z}_1 = -\omega_c z_1 + \omega_c k_1 z_1 + \omega_c k_2 z_2 \tag{57}$$

$$\dot{z}_2 = \frac{v_i}{C}\frac{z_1}{z_2} + \frac{L\omega_c}{C}\frac{z_1^2}{z_2} - \frac{L\omega_c k_1}{C}\frac{z_1^2}{z_2} - \frac{L\omega_c k_2}{C}z_1 - \frac{1}{RC}z_2. \tag{58}$$

To prove the stability of (57) and (58), consider the following candidate Lyapunov function:

$$V(z_1, z_1) = \frac{1}{2}Lz_1^2 + \frac{1}{2}Cz_2^2 > 0. \tag{59}$$

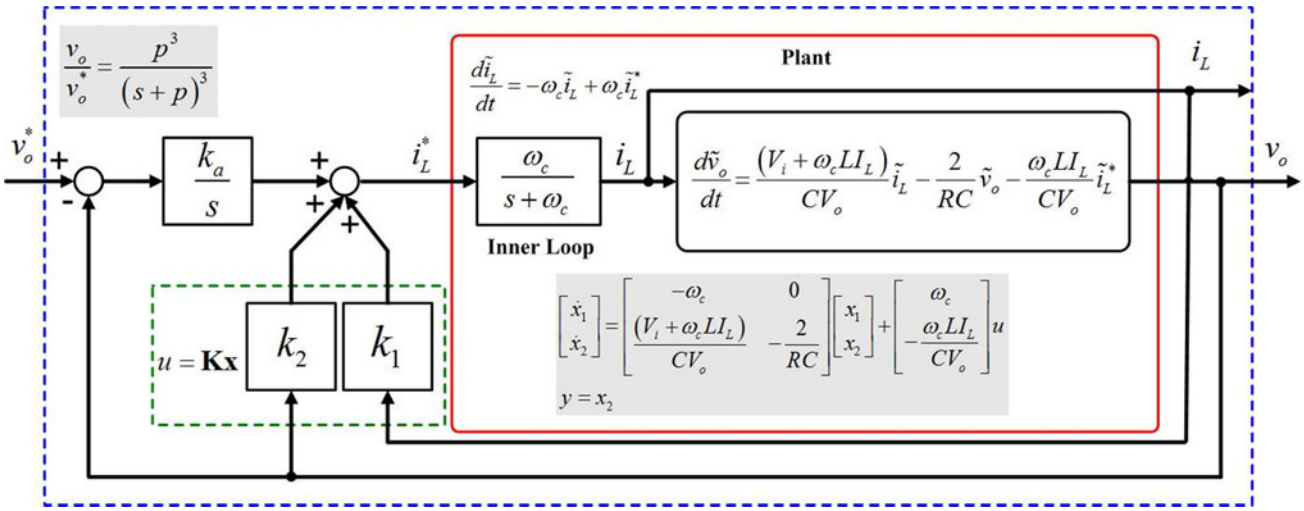

Fig. 18. Proposed state feedback control block diagram for voltage control.

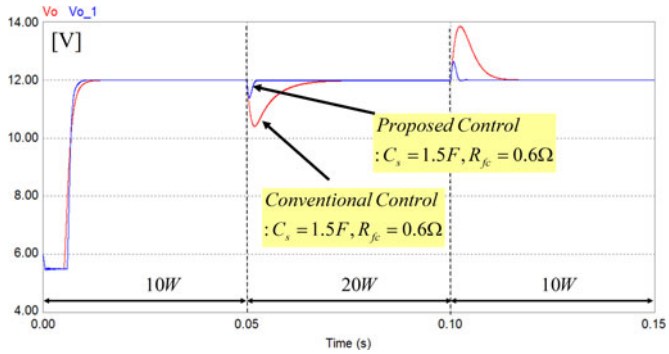

Fig. 19. Simulation waveform of transient response of proposed control and conventional control.

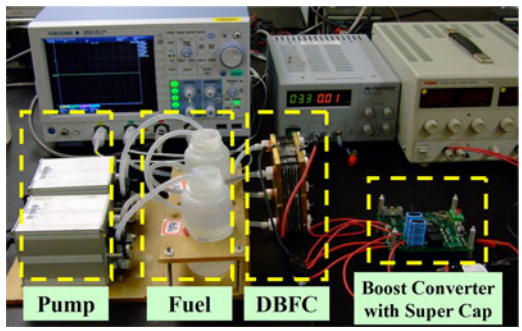

Fig. 20. Overall system configuration.

The time derivative of $V(z_1, z_1)$ is given as

$$\dot{V}(z_1, z_2) = Lz_1\dot{z}_1 + Cz_2\dot{z}_2 = v_i i_L - \frac{1}{R}v_o^2 = 0. \qquad (60)$$

Thus, it can be concluded that the stability of the closed-loop system is guaranteed in the proposed scheme.

VI. Simulation Results

Simulationswere carried out to verify the proposed analysis for the improvement of the response time by adding the supercapacitor and verify further response improvement of the proposed control. PSIM was used as a simulation tool. Fig. 19 shows the simulation waveforms of the transient response time of proposed control and conventional control. Comparing the proposed control and the conventional control, it is verified that the recovery time of the proposed control is improved by a factor of 4 times from 10 to 2.5 ms.

VII. Test Results

Fig. 20 shows overall system configuration. It consists of a pump, two fuel bottles, the DBFC, and the boost converter with integrated supercapacitor. For operation and control, the proposed current and voltage control loops are used.

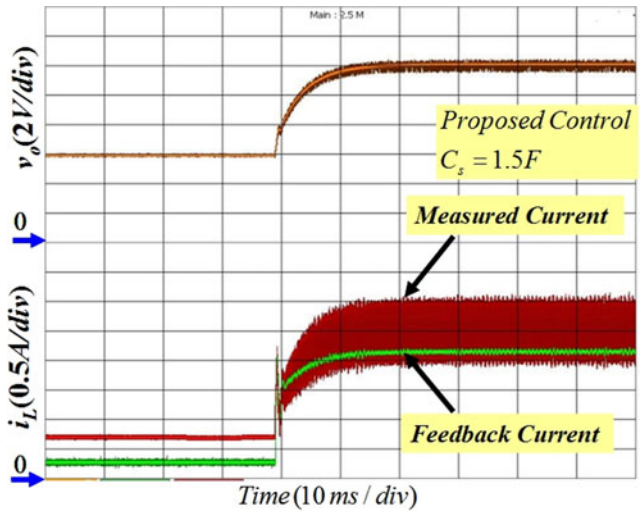

Fig. 21 Test waveform of step response in proposed control

The algorithms for the overall operation are designed with TI DSP (TMS32028035). The monitored states are the inductor current and the output voltage. In order to observe current clearly, a feedback current, which is the sampling current, is monitored because the inductor current has switching ripple.

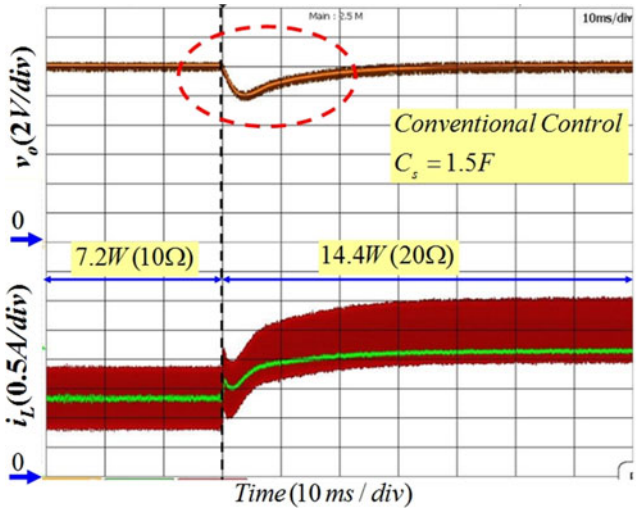

Fig. 22. Test waveform of transient response in conventional control.

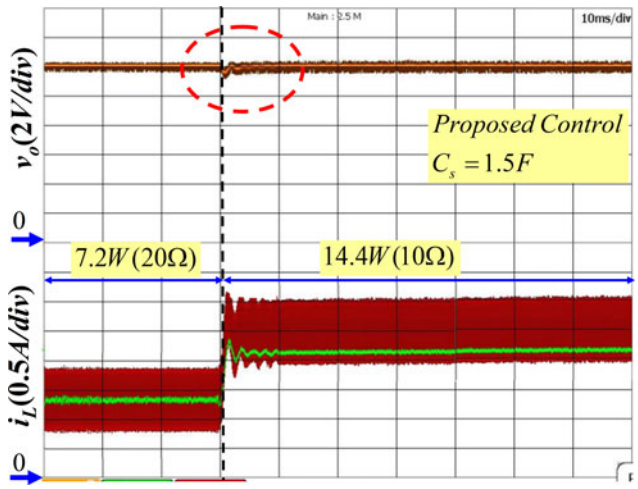

Fig. 23. Test waveform of transient response in proposed control.

Fig. 21 shows the test waveform of the step response in the proposed control. The reference voltage is 12 V. The response time to reach at steady state is about 10 ms. Therefore, the time constant is about 3.3 ms. Fig. 22 shows the test waveform of the transient response in the conventional control. The load is changed from 7.2 to 14.4 W. The recovery time for the load transition is about 20 ms and the under shoot voltage is –2 V. Fig. 23 shows the test waveform of the transient response in the proposed control. The recovery time for the load transition is about 2.5 ms and the under shoot voltage is –0.5 V. It is clear that the proposed control has further improved performance which is 12.5% better in terms of recovery time and 25% faster in the under shoot voltage. Therefore, it verified that the proposed control has high BW.

VIII. Conclusion

This paper analyzed the dynamic response of the dc–dc converter for fuel cell applications. Considering the model of the fuel cell power source, the response of the proposed feedforward-state feedback current control and voltage control are explained with Bode plots. In addition, this paper proposed to add a supercapacitor in order to increase the control response time. Two control schemes were proposed for the improvement of the BW. One is the nonlinear feedforward for current loop. The other is the state feedback control for voltage loop. The 20-W prototype DBFC power conditioning system was designed and used for the experiments to verify the proposed control methods.

The main contributions of this paper are as follows.

1) Derived the boost converter small signal modeling including the DBFC impedance.
2) Analyzed the impact of the impedance on the voltage and current control loops for the boost converter.
3) Explained the dc–dc converter design with fast response time by adding the supercapacitor.
4) Improved control loop BW with two proposed control schemes.

In addition, it showed the way of designing the digital controller for small portable power source with multiple control operations.

Acknowledgment

The authors would like to acknowledge Northeast Utilities Company for their financial support and creating this research opportunity. They are grateful to Dr. M. Anwar and Dr. P. Singh for their help in obtaining involvement in this project, and P. Menard for his knowledgeable and reliable assistance in all matter of tasks.

References

[1] K.-W. Suh and A. G. Stefanopoulou, "Coordination of converter and fuel cell controllers," in *Proc. IEEE Int. Symp. Int. Control, Mediterrean Conf. Control Autom.*, Jun.27–29, 2005, pp. 563–568.

[2] Z. Qian, O. Abdel-Rahman, and I. Batarseh, "An integrated four-port dc/dc converter for renewable energy applications," *IEEE Trans. Power Electron.*, vol. 25, no. 7, pp. 1877–1887, Jul. 2010.

[3] A. S. Samosir and A. H. M. Yatim, "Implementation of dynamic evolution control of bidirectional dc–dc converter for interfacing ultracapacitor energy storage to fuel-cell system," *IEEE Trans. Ind. Electron.*, vol. 57, no. 10, pp. 3468–3473, Oct. 2010.

[4] W. Liu, J. Chen, T. Liang, R. Lin, and C. Liu, "Analysis, design, and control of bidirectional cascaded configuration for a fuel cell hybrid power system," *IEEE Trans. Power Electron.*, vol. 25, no. 6, pp. 1565–1575, Jun. 2010.

[5] K. Jin, X. Ruan, M. Yang, and M. Xu, "A hybrid fuel cell power system," *IEEE Trans. Ind. Electron.*, vol. 56, no. 4, pp. 1212–1222, Apr. 2009.

[6] W.-S. Liu, J.-F. Chen, T.-J. Liang, and R.-L. Lin, "Multicascoded sources for a high-efficiency fuel-cell hybrid power system in high-voltage application," *IEEE Trans. Power Electron.*, vol. 26, no. 3, pp. 931–942, Mar. 2011.

[7] M. Harfman-Todorovic, M. Chellappan, L. Palma, and P. Enjeti, "The role of supercapacitors in designing fuel cell powered portable applications," in *Proc. IEEE Power Electron. Spec. Conf.*, Jun.15–19, 2008, pp. 2465–2472.

[8] J.-i. Itoh and F. Hayashi, "Ripple current reduction of a fuel cell for a single-phase isolated converter using a dc active filter with a center tap," *IEEE Trans. Power Electron.*, vol. 25, no. 3, pp. 550–556, Mar. 2010.

[9] M. H. Todorovic, L. Palma, and P. Enjeti, "Design of a wide input range dc–dc converter with a robust power control scheme suitable for fuel cell power conversion," in *Proc. IEEE 19th Annu. Appl. Power Electron. Conf. Expo.*, 2004, vol. 1, pp. 374–379.

[10] J.-C. Hwang, L.-H. Chen, and S.-N. Yeh, "A three-leg fuel-cell boost converter with novel digital-signal-processor based pulse-width modulation," in *Proc. IEEE Region 10 Conf. (TENCON)*, Oct. 30–Nov. 2, 2007, pp. 1–4.

[11] L. Palma, M. Harfman-Todorovic, P. Enjeti, and S. Choi, "Analysis of dc–dc converter stability in fuel cell powered portable electronic system," in *Proc. 37th IEEE Power Electron. Spec. Conf.*, Jun.18–22, 2006, pp. 1–6.
[12] Y. Kenarangui, S. Wang, and B. Fahimi, "On the impact of fuel cell system response on power electronics converter design," in *Proc. IEEE Vehicle Power Propulsion Conf.*, Sep. 2006, pp. 6–8.
[13] D. M. Van de Sype, K. De Gusseme, A. P. M. Van den Bossche, and J. A. Melkebeek, "Duty-ratio feedforward for digitally controlled boost PFC converters," *IEEE Trans. Ind. Electron.*, vol. 52, no. 1, pp. 108–115, Feb. 2005.
[14] D. M. V. Van de Sype, K. De Gusseme, A. P. Van den Bossche, and J. A. Melkebeek, "Duty-ratio feedforward for digitally controlled boost PFC converters," in *Proc. 18th Annu. IEEE Appl. Power Electron. Conf. Expo.*, vol. 1, pp. 396–402, Feb. 9–13, 2003.
[15] J. Liu, W. Ming, and F. Gao, "A new control strategy for improving performance of boost dc/dc converter based on input-output feedback linearization," in *Proc. 8th World Congr. Intell. Control Autom.*, Jul.7–9, 2010, pp. 2439–2444.
[16] Z. Chen, W. Gao, J. Hu, and X. Ye, "Closed-loop analysis and cascade control of a nonminimum phase boost converter," *IEEE Trans. Power Electron.*, vol. 26, no. 4, pp. 1237–1252, Apr. 2011.
[17] W. Ming and J. Liu, "A new experimental study of input-output feedback linearization based control of Boost type dc/dc converter," in *Proc. IEEE Int. Conf. Ind. Technol.*, Mar.14–17, 2010, pp. 685–689.
[18] D. Shuai, Y. Xie, and X. Wang, "The research of input-output linearization and stabilization analysis of internal dynamics on the CCM Boost converter," in *Proc. Int. Conf .Electr. Mach. Syst.*, Oct.17–20, 2008, pp. 1860–1864.
[19] M. J. Tarca, T.-S. Hwang, and S.-Y. Park, "Design and operation of an autonomous fuel cell-supercapacitor power system for portable applications," in *Proc. IEEE 8th Int. Conf. Power Electron. ECCE Asia (ICPE & ECCE)*, May 30–Jun. 3, 2011, pp. 2367–2373.
[20] X. Zhou and S.-Y. Park, "Design and analysis of a direct borohydride fuel cell dc–dc converter for portable applications," in *Proc. ASME 8th Int. Fuel Cell Sci. 7 Technol. Conf.*, Jun. 14–16, 2010, Brooklyn NY.
[21] R. Li, T. O'Brien, J. Lee, and J. Beecroft, "A unified small signal analysis of dc–dc converters with average current mode control," in *Proc. IEEE Energy Convers. Congr. Expo.*, Sep. 20–24, 2009, pp. 647–654.
[22] Y. W. Lu, G. Feng, and Y.-F. Liu, "A large signal dynamic model for dc-to-dc converters with average current control," in *19th Annu. IEEE Appl. Power Electron. Conf. Expo.*, 2004, vol. 2, pp. 797–803.
[23] W. Tang, F. C. Lee, and R. B. Ridley, "Small-signal modeling of average current-mode control," *IEEE Trans. Power Electron.*, vol. 8, no. 2, pp. 112–119, Apr. 1993.
[24] J. Ejea-Marti, E. Sanchis-Kilders, E. Maset, A. Ferreres, J. M. Blanes, A. Garrigos, J. Jordan, and V. Esteve, "Phase margin degradation of a peak current controlled converter at reduced duty cycle," *IEEE Trans. Power Electron.*, vol. 25, no. 4, pp. 863–874, Apr. 2010.
[25] J. Li and F. C. Lee, "New modeling approach and equivalent circuit representation for current-mode control," *IEEE Trans. Power Electron.*, vol. 25, no. 5, pp. 1218–1230, May 2010.
[26] A. Cantillo, A. De Nardo, N. Femia, and W. Zamboni, "Stability issues in peak-current-controlled SEPIC," *IEEE Trans. Power Electron.*, vol. 26, no. 2, pp. 551–562, Feb. 2011.
[27] K. Viswanathan, R. Oruganti, and D. Srinivasan, "Tri-state boost converter with no right half plane zero," in *Proc. 4th IEEE Int. Conf. Power Electron. Drive Syst*, Oct. 22–25, 2001, vol. 2, pp. 687–693.
[28] J. Calvente, L. Martinez-Salamero, H. Valderrama, and E. Vidal-Idiarte, "Using magnetic coupling to eliminate right half-plane zeros in boost converters," *IEEE Power Electron. Lett.*, vol. 2, no. 2, pp. 58–62, Jun. 2004.
[29] K. Viswanathan, R. Oruganti, and D. Srinivasan, "A novel tri-state boost converter with fast dynamics," *IEEE Trans. Power Electron.*, vol. 17, no. 5, pp. 677–683, Sep. 2002.
[30] S. Kapat, A. Patra, and S. Banerjee, "A current-controlled tristate boost converter with improved performance through RHP zero elimination," *IEEE Trans. Power Electron.*, vol. 24, no. 3, pp. 776–786, Mar. 2009.
[31] C.-T. Che, *Linear System Theory and Design*, 3rd ed. New York: Oxford Univ. Press, 1998.

Tai-Sik Hwang (S'11) received the B.S. and M.S. degrees in electrical engineering from Yeungnam University, Kyungbuk, Korea, in 2004 and 2006, respectively. He is currently working toward the Ph.D degree at the University of Connecticut, Storrs.

In 2006, he was with Robostar Company, Ltd.,where he worked on the servo motor drives for six axes industrial robot. In 2007, he became an Associate Researcher in POSCON R&D Center, Seoul, South Korea, where he worked on the power conditioning system for molten carbonate fuel cell generation system for two years. Since 2010, he has also been a Research Assistant in Center for Clean Energy Engineering, University of Connecticut. His research interests include grid-connected inverters, dc–dc converters, electrical motor drives and microgrids.

Matthew James Tarca (S'08) received the B.S. degree in electrical and computer engineering from the University of Connecticut, Storrs, in 2005, where he is currently working toward the Ph.D degree.

In 2008, he was with the Hamilton Sundstrand of Windsor Locks, Connecticut, where he worked in the Engine and Control Systems Department, developing automated tests. In 2010, he was a Research Assistant in the Center for Clean Energy Engineering, University of Connecticut. In 2011, he was a Consultant for EcoAir, Hamden, Connecticut and developed a digital controller for their high-power vehicle alternators. His research interests include electric vehicles, electrical motor drives, and embedded control.

Sung-Yeul Park (S'04–M'09) received the M.S. and Ph.D. degrees in electrical and computer engineering from the Virginia Polytechnic Institute and State University (Virginia Tech), Blacksburg, in 2004 and 2009, respectively.

From 2002 to 2004, he was a Graduate Research Assistant in Center for Rapid Transit Systems (CRTS), Virginia Tech. From 2004 to 2009, he was a Graduate Research Assistant in the Future Energy Electronics Center, Virginia Tech. In 2009, he was with the Department of Electrical and Computer Engineering, University of Connecticut, Storrs, as an Assistant Professor and also with the Center for Clean Energy Engineering, University of Connecticut, as an Associate Member. His research interests include energy efficient conversion, distributed generation integration, smart building, and microgrid applications.

Dr. Park received several international paper awards including the Third Paper Award in IAS 2004, the IPCC 2007 Best Paper Award, an outstanding writing award in the International Future Energy Challenge in 2007 and the Torgersen Research Excellence Award at College of School in Virginia Tech in 2009.